

Supporting Information

Formation of correlated chromatin domains at nanoscale dynamic resolution during transcription

Haitham A. Shaban^{§, #}, Roman Barth^{§, &}, Kerstin Bystricky[#]

Laboratoire de Biologie Moléculaire Eucaryote (LBME), Centre de Biologie Intégrative (CBI), CNRS; University of Toulouse, UPS; 31062 Toulouse; France

&- Present address: Faculty of Applied Sciences, Delft University of Technology; 2628 CJ Delft; The Netherlands; §: authors contributed equally

#: corresponding author: haitham.shaban@ibcg.biotoul.fr, kerstin.bystricky@ibcg.biotoul.fr

Content:

Supplementary Note 1

This section provides information about Optical Flow and the methods compared in the article. We introduce the methods' basics, highlight their key features and limitations as far as they are known/available. Tables in this section summarize the most important variables and give an overview over the methods.

Table 1: The most important variables and their meaning used throughout this document.

Table 2: Method overview.

This note also provides details about simulated parameters concerning microscopic and dynamic properties.

Supplementary Note 2

This note provides additional information about correlation on circular variables, the correlation model and the smoothness parameter.

Supplementary Figures

Figure S1: Simulated data and example response of motion estimated by the investigated methods.

Figure S2: Angle definition on a linear scale.

Figure S3: Interpretation of the smoothness parameter by the Whittle-Matern model.

Figure S4: Representative flow fields and magnifications.

Supplementary Note 1

Optical Flow algorithms estimate the flow field between two images such that the displacement meets $I(x + u, y + v, t + \Delta t) = I(x, y, t)$ where $I(x, y, t)$ is the brightness pattern at time t and $\vec{V}(x, y) = [u(x, y), v(x, y)]^T$ is the flow field between a frame at time t and a frame at time $t + \Delta t$. The original formulation of Optical Flow by Horn and Schunck (HS) (1) and Lucas and Kanade (LK) (2) was continuously further developed to seek greater accuracy (e.g. 3, 4). However, many modern methods are still based on the original formulation for which two main assumptions have to be made. First, it is assumed that brightness stays constant across a pair of images and only the brightness distribution changes due to the underlying motion. Second, one assumes piecewise smoothness of the underlying flow field. The brightness constancy assumption is a strict constraint and can often not be met in real applications (e.g. due to illumination changes, spot appearance and disappearance or noise). This issue is circumvented by solving the optimization problem in an iterative pyramidal (coarse-to-fine) scheme. Input images are down-sampled and the flow field is estimated on a coarse level. At the next finer level, the computed flow field is used to warp the second image towards the first one; the flow increment between the first image and the warped second image is calculated to refine the flow field. Due to down-sampling, images are blurred and small violations to the brightness constancy constraint become less important.

Table 1 lists the most important variables used throughout this document.

Variable	Meaning
$I_{1/2}$	Intensity distribution of image 1 and 2, respectively
$\vec{V} = (u, v)^T$	Flow field with horizontal component u and vertical component v
λ	Regularization parameter
$\vec{x} = (x, y)^T$	Spatial coordinate
$\rho(\cdot)$	Penalty function
$\nabla = \left(\frac{\partial}{\partial x}, \frac{\partial}{\partial y} \right)^T$	(Two-dimensional) Nabla operator
$(\cdot, \cdot)^T$	Transposed vector/matrix

Table 3: The most important variables and their meaning used throughout this document.

Method ID	Key features	Reference
1	HS-based, coarse-to-fine scheme, intermediate median filtering, motion discontinuity preserving, generalized Charbonnier penalty	(3)
2	LK-based, no coarse-to-fine scheme	(5)
3a	PIV (region-based matching), window size 16x16	(6)
3b	PIV (region-based matching), window size 8x8	(6)
3c	PIV (region-based matching), window size 4x4	(6)
4	Phase-based, neural network solver for component constraints	(7)
5	SIFT-based, motion discontinuity preserving, coarse-to-fine scheme	(8)

Table 4: Method overview. The five methods under considerations are listed with their corresponding method ID, references to publications and key features.

Method 1

Introduction

Sun *et al.* (3) give an extensive review of current Optical Flow methods and explore main principles behind them. Using a baseline-method, current practices are systematically varied to probe their influence on the method’s accuracy. The key point of their proposed approach is that median filtering of interim flow fields is needed during the optimization process. The penalty function in the objective function is chosen to be a slightly non-convex generalized Charbonnier function.

Fundamental Functionality

The authors apply the Rudin-Osher-Fatemi (9) structure texture decomposition against illumination changes to the input images. Optical Flow is estimated in a coarse-to-fine manner. The objective function to be minimized is written as

$$E(\vec{V}) = \sum_{\vec{x}} \rho \left(I_1(\vec{x} + \vec{V}) - I_2(\vec{x}) \right) + \lambda \rho(\nabla \vec{V}) \quad (1)$$

Where $\rho(x) = (x^2 + \epsilon^2)^{0.45}$, with $\epsilon = 0.001$, is the slightly non-convex generalized Charbonnier penalty function for both the data and the smoothness term. Based on the authors’ comparative analysis, this penalty function provides the highest accuracy in their training set. The slight non-convexity of the penalty function guarantees robustness to outliers. Spatial derivatives are calculated

using a spline-based implementation of bicubic interpolation with a 5-point filter which is shown to give the lowest energy solutions. A key point in Optical Flow estimation is found by the authors to consist in median filtering of intermediate flow fields with a 5x5 filter size in order to improve accuracy significantly. However, median filtering can result in over-smoothing when a neighborhood is centered on a small or thin structure and the surrounding area dominates. Formulating the median filtering practice explicitly as an objective function allows to improve the objective function by introducing a spatial weight to the filtering. The weight is defined according to each pixel's spatial distance, their brightness values and the unknown flow field (by using the latest estimate) explicitly. Using a Sobel edge detector, flow boundaries are obtained and smoothing across boundaries is reduced.

Conclusion/Limitations

The authors develop their algorithm based on a combination of current practices in Optical Flow estimation. Their comparative analysis allows them to consider accuracy ameliorating principles – median filtering as a key point. The explicit formulation of the heuristic filtering as an objective function achieves further improvement in filtering by detecting image and flow boundaries. The authors state that their algorithm produces larger errors on occlusion regions and that small, fast moving objects cause problems.

Method 2

Introduction

An early approach suggested by Lucas and Kanade (2) is further developed in order to overcome the so-called aperture problem of Optical Flow. Their algorithm is simple and very fast in computation of dense flow fields and finds application in the real-time analysis of lip motion and lip segmentation.

Fundamental Functionality

The original formulation of LK (2), is not suitable in regions of badly distributed structures, i.e. in regions where image gradients are linearly dependent.

$$E(\vec{V}) = \sum_{\vec{x}} \left(\frac{\partial I}{\partial t} + \vec{V} \nabla I \right)^2 \quad (2)$$

This is called the aperture problem. To overcome this issue, the authors apply an equation in which the normal flow at a single point is given by

$$\vec{V}_n = -\frac{\nabla I}{|\nabla I|^2} \frac{\partial I}{\partial t} \quad (3)$$

And thus line flow can be computed by averaging the normal flow over a region. Equations (2) and (3) perform well for point motion and line motion respectively. A weighted combination of both resulting flow vectors yields a reliable estimate of linear symmetry. The weighting between them consists in a factor depicting the amount of linear symmetry derived by an eigenvalue analysis of the two-dimensional structure tensor. However, the resulting system is ill-posed for the case of linear symmetry. Applying a Tikhonov regularization (adding a small positive value in order to avoid the “divide by zero” problem) resolves this issue, but simultaneously introduces a bias for smaller solutions by artificially raising the error minimized.

Conclusion/Limitations

The authors present a way to overcome the aperture problem in Optical Flow estimation by introducing the structure tensor to the LK formulation. The need for a fast implementation keeps the algorithm simple and a coarse-to-fine estimation is renounced, which causes problems in case of large displacements. The obligatory Tikhonov regularization favors smaller solutions, introducing a bias.

Method 3

Introduction

Particle Image Velocimetry (PIV) uses pattern matching in corresponding sub-regions of two input images in order to quantitatively measure fluid velocity vectors at a large number of points simultaneously (10).

Fundamental Functionality

Two input images are divided into smaller sub-regions of given size. Each sub-region in the first image is compared to the corresponding sub-region in the second image by calculating the cross-correlation between them. The position of the correlation peak corresponds to the vector by which the pattern in the sub-region in image 1 is displaced in respect to image 2. The image is scanned until a displacement vector is found for every sub-region. Overlapping sub-regions produce a dense and usually smooth flow field. The accuracy of estimated flow fields is enhanced by scanning the image iteratively with sub-regions of decreasing size until the desired window size is reached. The estimation of each iteration is used in the following to refine the flow field. Possibly spurious vectors

are filtered if the signal-to-noise ratio in the correlation peak or the correlation peak height is too small to be reliable, by a median filter and by a global filter, which removes significantly larger or smaller vectors than the majority.

Window sizes of 16x16 (method 3a) of 8x8 (method 3b) and of 4x4 (method 3c) pixels are used.

Conclusion/Limitations

Images are divided into sub-regions and scanned to construct a flow field. Overlapping regions and iterative refinement allows to construct a dense flow field. Overlapping and filtering usually produces reasonably smooth fields despite an explicit smoothness constraint that is not taken into consideration. In case of noisy data, exact determination of the correlation peak is difficult and might lead to erroneous results. It is assumed that a pattern within the window is displaced from image 1 to 2, but changes inside the interrogation window are not considered.

Method 4

Introduction

The method is a phase-based approach to estimate flow fields using spatial filtering. Instead of contours of constant amplitude, contours of constant phase are tracked. Several component velocities are estimated using quadrature Gabor filter pairs and the component velocities are connected to a constraint of the full velocity. The full velocity, which is consistent with all constraints, is calculated by a recurrent neural network.

Fundamental Functionality

The convolution of an input image with a 2D Gabor filter

$$G(\vec{x}, \vec{f}) = \exp\left(-\frac{|\vec{x}|^2}{\sigma^2}\right) \exp(2\pi i \vec{x} \vec{f}) \quad (4)$$

with peak frequency $\vec{f} = (f_x, f_y)^T$ and the width of the Gaussian σ results in a complex-valued filter response. The phase ϕ of the filter response can be used to estimate the Optical Flow under the assumption that constant phase surfaces evolve according to the flow field (11). The phase gradient constraint is an analogue to the gradient constancy assumption in differential Optical Flow methods (12):

$$\nabla \phi \cdot \vec{V} + \frac{\partial \phi}{\partial t} = 0 \quad (5)$$

Due to the aperture problem, only the normal flow component can be computed which are referred to as component velocities. The temporal linearity of the phase is used as a confidence measure. It is expected that an unreliable phase information is unstable over time and therefore does not propagate linearly leading to rejection of non-linearly evolving phase information. A component velocity is calculated for a set of 11 filter pairs and the full velocity can be determined by the remaining component velocities in one point. The full velocity is constrained by every component velocity to lie on a “constraint line” in the velocity space. A recurrent neural network performs the optimization process and finds the full velocity based on several constraints.

Conclusion/Limitations

At every spatial location, several component velocities are calculated using constant phase contours. Nonlinearity in the phase propagation serves as reliability measure and the full velocity can be determined by several constraints. Phase-based methods are more robust to illumination changes as well as deviations from pure translation than amplitude-based methods (11). However, in the framework of two-image optical flow estimation, the linearity measure breaks down and no filtering of component velocities can occur compromising accuracy of the method.

Method 5

Introduction

The algorithm uses densely sampled SIFT descriptors (13, 14) and matches them between two images. The method preserves spatial discontinuities while the objective function is subject to decoupled smoothness terms. The images do not necessarily have to originate from the same image sequence, but can consist of two images of the same object category.

Fundamental Functionality

SIFT descriptors are extracted at every pixel of the input images. In order to match SIFT descriptors between images, the following objective function is minimized (the notation $|\cdot|$ defines the L_1 -norm):

$$\begin{aligned}
E(\vec{V}) = & \sum_{\vec{x}} \min(|s_1(\vec{x}) - s_2(\vec{x} + \vec{V})|, t) + \sum_{\vec{x}} \eta(|u(\vec{x})| + |v(\vec{x})|) \\
& + \sum_{\vec{x}, \vec{x}' \in N} \min(\alpha|u(\vec{x}) - u(\vec{x}')|, d) \\
& + \sum_{\vec{x}, \vec{x}' \in N} \min(\alpha|v(\vec{x}) - v(\vec{x}')|, d)
\end{aligned} \tag{6}$$

where $s_i(\vec{x})$ is the SIFT descriptor extracted at \vec{x} in image i , N is a 4x4 neighborhood, η and α are fixed regularization parameters and d and t are threshold values. The objective function consists of the data term, in which the SIFT descriptors are constrained to be matched with the displacement vector and the L_1 -norm accounts for outliers and motion discontinuities. The second term consists of a penalty on the vector's magnitude. Note that no constraint is given for the length of vectors (they could span a range as large as the image itself), but the smallest possible solution is favored. The third and fourth term are smoothness terms. The threshold regularization above preserves motion discontinuities. Vector components u and v are restricted to be integers in the authors' implementation. The objective function is directly optimized by a Belief Propagation (15) in a coarse-to-fine matching.

Conclusion/Limitations

The method does not make use of typical assumptions in Optical Flow estimations as brightness constancy and piecewise smoothness of the flow field. Instead, dense SIFT descriptors are used to match two images. No constraints exist in the magnitude of displacements and therefore any pixel in the first image can be matched to any other pixel in the second image. For the use of biological data, sampled at short time lags these large displacements may be spurious. However, favoring small displacements partially prevents this issue. The use of threshold regularization preserves motion discontinuities.

Simulated parameters

Microscopic properties: We examine the accuracy of different algorithms based on the variation of the labeling density and the Signal-to-Noise ratio (SNR). Note that emitters are not placed near the border in order to avoid boundary effects. The imaging process can be modeled by the convolution of the emission with the point spread function (PSF) of the microscopic setup, which is assumed to be space-invariant. Emitters are added sequentially to the image and each of the emitter's spatial contribution to the pixel intensity is described by the integrated form of a symmetric 2D Gaussian

function representing the PSF. The intensity value at the integer pixel position $(x, y)^T$ is expressed as (16).

$$v(x, y|\hat{x}, \hat{y}, \sigma) = E_x E_y, \quad (7)$$

$$E_x(x, y|\hat{x}, \hat{y}, \sigma) = \frac{1}{2} \operatorname{erf}\left(\frac{x - \hat{x} + \frac{1}{2}}{\sqrt{2}\sigma}\right) - \frac{1}{2} \operatorname{erf}\left(\frac{x - \hat{x} - \frac{1}{2}}{\sqrt{2}\sigma}\right), \quad (8)$$

$$E_y(x, y|\hat{x}, \hat{y}, \sigma) = \frac{1}{2} \operatorname{erf}\left(\frac{y - \hat{y} + \frac{1}{2}}{\sqrt{2}\sigma}\right) - \frac{1}{2} \operatorname{erf}\left(\frac{y - \hat{y} - \frac{1}{2}}{\sqrt{2}\sigma}\right), \quad (9)$$

where $(\hat{x}, \hat{y})^T$ defines the sub-pixel coordinates within a circle of radius 3σ and center $(x, y)^T$ and $\sigma = 0.8 \text{ px}$ is the standard deviation of the 2D Gaussian function approximating the PSF.

As we are modeling a photon counting process, the image data is subject to Poisson noise. We define the SNR by $SNR = I_{max}/I_0$ with I_{max} denoting the peak (particle) intensity and I_0 the mean background intensity. The SNR is varied from ∞ (no noise) to 30.

Dynamic properties: Chromatin within interphase is organized into regions of functional domains. Some of these domains might undergo coherent motion. The accuracy of OF methods can be estimated by their capability to distinguish between these domains. Domains of particles undergoing diffusion in the same direction and magnitude were simulated by placing random disks of appropriate diameter in the image plane. Particles placed randomly in the same domain are forced to undergo the same displacement. Therefore, we modeled different numbers of coherently moving domains, ranging from 1 up to 50, including the number of chromosomes in human cells.

For a two-frame OF estimation, we vary the distance by which each emitter travels per frame. Motion of emitters in every domain is independently modeled as Brownian motion, i.e. drawn from a normal distribution with zero mean and variance $\sigma^2 = 4D\tau$ for the two-dimensional case (17) where D is the diffusion coefficient and $\tau = 0.2 \text{ s}$ is the acquisition time between subsequent images. The diffusion coefficient is empirically varied from 0.1 to 4 px^2/frame corresponding to emitters moving about 0.6 pixels up to 4 pixels per frame. These values correlate well with previously found dynamics of chromatin under various conditions (18, 19). The simulated motion is the ground-truth to which estimated flow fields are compared and quantitatively evaluated.

Supplementary Note 2

Correlation on circular variables: To study the potential extent of coherent motion, we calculate the spatial autocorrelation of sets of angles $\gamma(x, y)$ of a given flow field $\vec{V}(\vec{r})$. Angles are calculated by the arctangent of the y- and x-component of a given vector

$$\gamma = \begin{cases} \arctan(v/u) & \text{if } u \geq 0, \\ \arctan(v/u) + \pi & \text{if } u < 0, v \geq 0, \\ \arctan(v/u) - \pi & \text{if } u < 0, v < 0, \\ 0 & \text{if } u > 0, v = 0, \\ \pi & \text{if } u < 0, v = 0, \\ \text{undefined} & \text{if } u = 0, v = 0. \end{cases}, \quad (10)$$

Angles calculated by equation **Erreur ! Source du renvoi introuvable.** are defined on the linear interval $(-\pi, \pi)$, where the positive x-axis is arbitrarily chosen as a reference. Note that the definition of angles on a linear interval introduces errors in the spatial correlation between certain angles. In particular, consider two vectors \vec{V}_1 and \vec{V}_2 of unit length pointing approximately in negative x-direction, where \vec{V}_1 has a small, positive y-component and \vec{V}_2 has a small, but negative y-component (Supplementary FigureS2). Following equation **Erreur ! Source du renvoi introuvable.**, the angles of the two vectors \vec{V}_1 and \vec{V}_2 will be $\gamma_1 = \pi - \epsilon$ and $\gamma_2 = -\pi + \epsilon = -\gamma_1$ and their difference is $|\gamma_1 - \gamma_2| = 2\pi - 2\epsilon$, where ϵ is small, due to the branch cut along the negative x-axis. The angle difference between these two vectors is large, however the vectors point approximately in the same direction. To overcome this issue, the true angle values are expressed in the complex plane using Euler's formula $e^{i\gamma} = \cos \gamma + i \sin \gamma$, where $i = \sqrt{-1}$. In this description, the difference between the angles reduces to $|\gamma_1 - \gamma_2| = 2i\epsilon_2$, where ϵ_1 and ϵ_2 are small.

Correlation model: A recent study has investigated the correlated motion of chromatin and found empirically that the directional correlation follows a power law with exponential cut off (18):

$$r(\rho) \propto \rho^a \exp\left(-\frac{\rho}{\rho_c}\right). \quad (11)$$

where ρ_c is the correlation length and a is a scaling parameter. For increasing spatial distance between two points, the correlation decreases and tends to zero for $\rho \rightarrow \infty$. Extrapolation to zero space lag fails in this model as

$$\lim_{\rho \rightarrow 0} r(\rho) = \begin{cases} 0 & \text{if } a > 0 \\ \infty & \text{if } a < 0 \end{cases}. \quad (12)$$

We therefore apply the Whittle-Màtern (WM) model, which ranges from a simple exponential decay ($\nu = 1/2$) to a Gaussian ($\nu \rightarrow \infty$) and can therefore be seen as a generalization of several correlation

models. For $\nu \sim m + 1/2$, $m \in \mathbb{N}$ and positive, the WM model takes the form of an exponential decay over a polynomial of order m (20, 21), in particular:

$$\nu = \frac{1}{2}, \quad r(\rho) \propto \exp\left(-\frac{\rho}{\rho_c}\right) \quad (134)$$

$$\nu = \frac{3}{2}, \quad r(\rho) \propto \left[\frac{\rho}{\rho_c} + 1\right] \cdot \exp\left(-\frac{\rho}{\rho_c}\right) \quad (145)$$

$$\nu = \frac{5}{2}, \quad r(\rho) \propto \left[\left(\frac{\rho}{\rho_c}\right)^2 + 3\frac{\rho}{\rho_c} + 3\right] \cdot \exp\left(-\frac{\rho}{\rho_c}\right) \quad (156)$$

$$\nu \rightarrow \infty, \quad r(\rho) \propto \exp\left(-\frac{\rho^2}{\rho_c^2}\right) \quad (76)$$

Smoothness parameter: The smoothness parameter allows for considerable flexibility in describing the empirical correlation because it covers a wide range of functions. A spectator regarding several two-dimensional scalar fields visually might argue that one field is smoother than another. Featureless areas are considered as smooth while abrupt changes of values, i.e. the boundary of an object in an image, are called rough. A rough change of values in spatial proximity is related to the spatial gradient. Large values in the gradient field denote large changes between adjacent variables and transitions between these are rough. The smoothness parameter is therefore small. An illustrative example of the behavior of the smoothness parameter ν in respect to smooth and rough fields is given in (Figure S3). An U2OS cell nucleus expressing H2B-GFP is analyzed by the Horn-Schunck based and SIFT-based method and their scalar field depicting the local direction of the flow field is color-coded in (Figure S3a). The horizontal gradient is shown exemplary in (Figure S3b), color coded from blue to red corresponding to a change in angle from $-\pi$ to π . For the HS-based method, distinct lines can be seen indicating boundaries between coherently moving regions of chromatin (Figure S3b). The values of the gradient fields are presented as histograms for the horizontal gradient (red) and the vertical gradient (green) in (Figure S3c). The characteristic peak around zero indicates that most of the fields correspond to smooth, i.e. spatially slowly varying motion. However, large changes in direction increase among the flow fields from top to bottom and therefore the overall variance σ^2 of the gradient fields increases accordingly. The rise in the variance of gradient fields, i.e. larger differences in directions of nearby pixels and therefore sharp and frequent boundaries cause a low smoothness parameter ν as calculated from the regression of the fields' correlation function.

Supplementary Figures

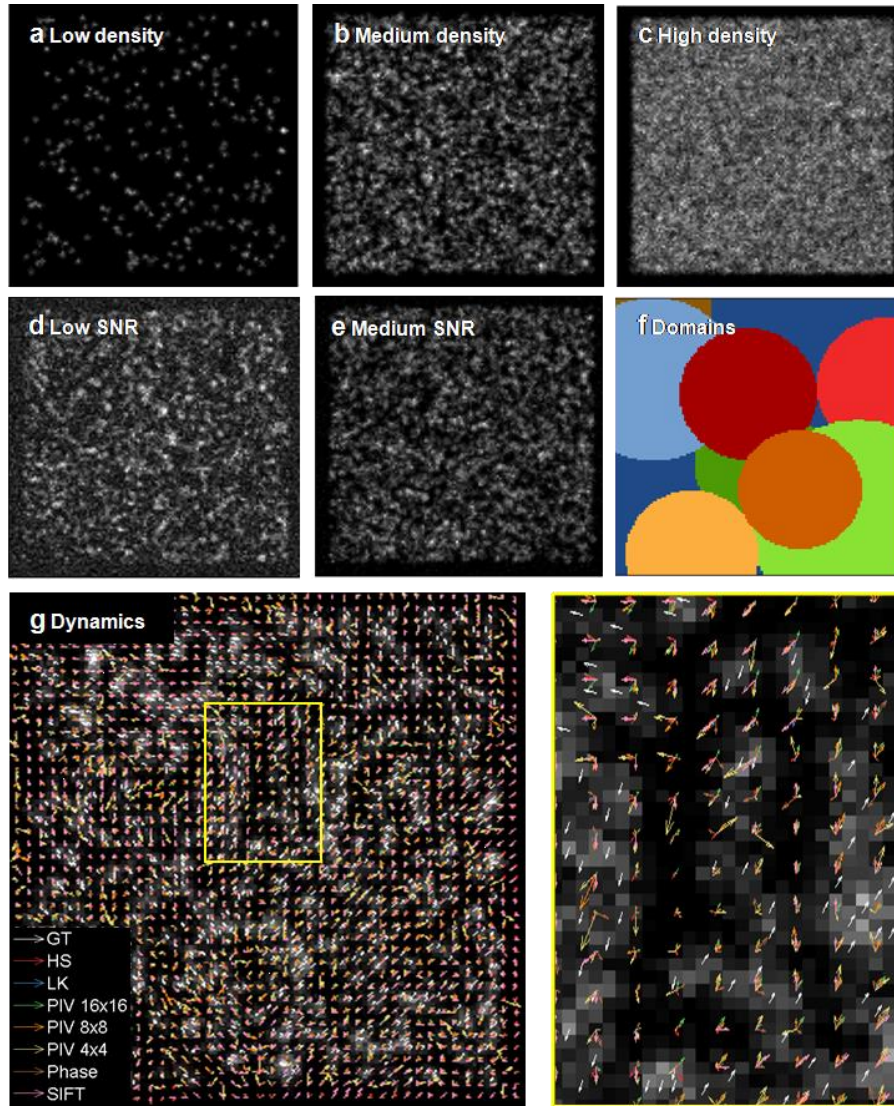


Figure S1: Simulated data and example response of motion estimated by the investigated methods. Simulated data are 128x128 pixels and emitters are randomly placed in the plane except at the border. **a-c)** Low (0.02 px^{-1}), medium (0.25 px^{-1}) and high (2.5 px^{-1}) density of emitters without noise. **d-e)** Medium density and low (5) and medium (30) signal-to-noise ratio. The case of high SNR corresponds to **a-c**. **f)** Simulated domains placed randomly in the image plane. Different colors correspond to different labels of the domains, each exhibiting independent motion. The domains are modeled as circles with varying diameter, where the diameter is adjusted with respect to the number of domains. The example is shown for 10 domains with average radius of 35 pixels. **g)** First frame of a simulated pair with intermediate emitter density and no noise. The ground truth motion (GT, white arrows) and the estimations by the methods under considerations are overlaid. For clarity, estimated fields are subsampled such that every third vector is shown only. Colors correspond to different methods as indicated in the legend. A magnified view of the yellow rectangle is shown on the right. Note that the GT is sparse (only available at the positions of emitters), whereas the reconstruction methods give dense fields as no determination on the position of emitters is done. The methods are consistent in regions of coherent flow (e.g. at the lower right), whereas motion boundaries cause more variance among the methods (e.g. at the center of the enlarged area).

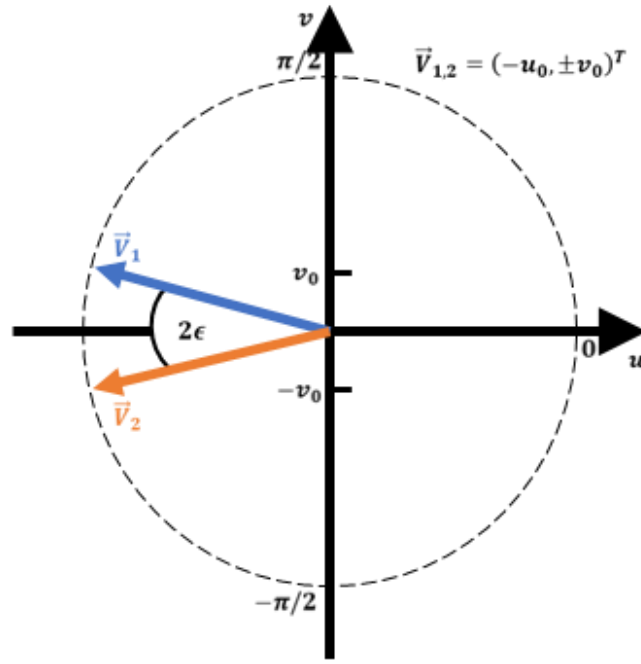


Figure S2: Definition of angles on a linear scale. Let two vectors \vec{V}_1 and \vec{V}_2 of unit length point in approximately the negative x-direction. The branch cut is defined at the negative x-axis. The difference between the angles of the two vectors is $2\pi - 2\epsilon$, with ϵ small. However, due to the periodicity of 2π , the difference can also be calculated to 2ϵ .

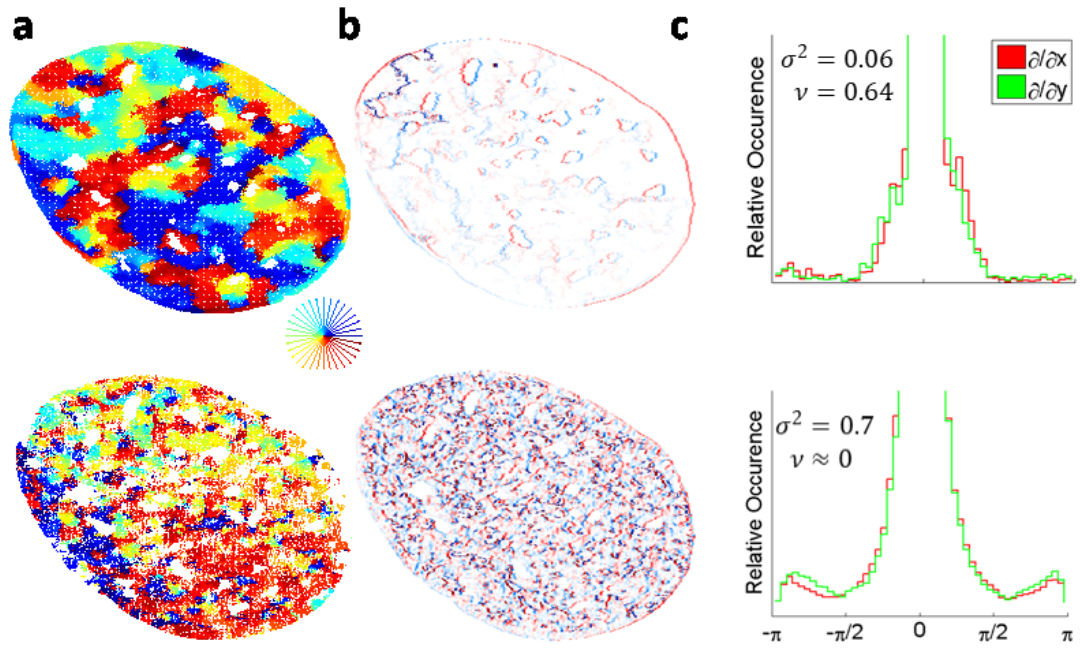


Figure S3: Interpretation of the smoothness parameter in the Whittle-Màtern model. **a)** The flow field of an example U2OS cell expressing H2B-GFP is shown for the Horn-Schunck and SIFT-based method. Colors correspond to the direction of vectors. Inspection of the flow fields by eye leads to the conclusion that the smoothness of the fields decreases from top to bottom. **b)** The horizontal gradient of the direction is shown for the two methods. The gradient fields are color-coded from blue to red corresponding to change in direction from $-\pi$ to π between nearby pixels. **c)** Representation of the horizontal (red) and vertical (green) gradient fields as histogram. An overall increase in the variance of the gradient fields corresponds to a decrease of the smoothness parameter.

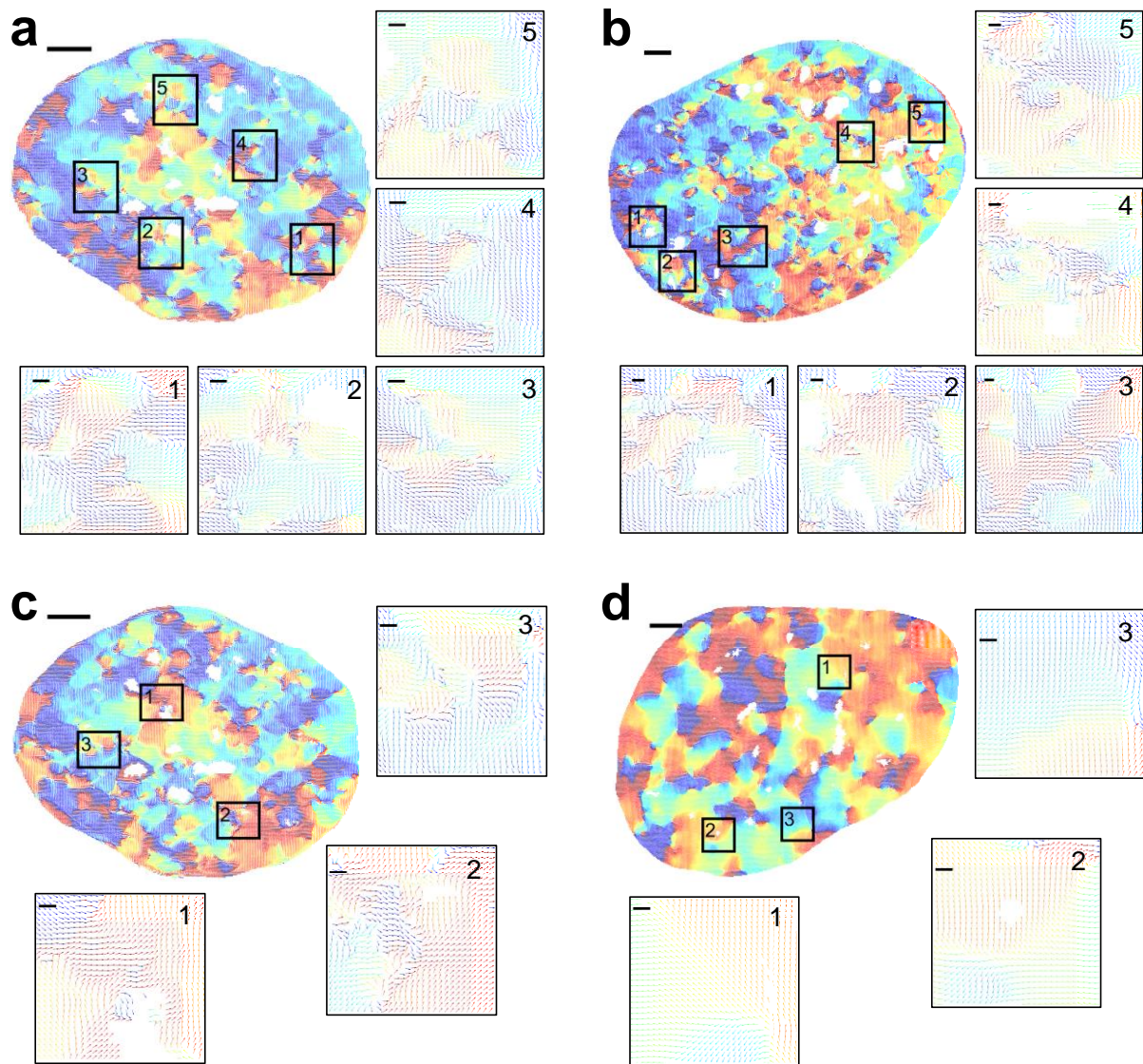


Figure S4: Representative flow fields. **a)** Mean direction over 30 s of H2B tagged GFP and **b)** DNA respectively in a representative U2OS nucleus. Example regions of converging flow (vortices) are enlarged. **c)** Visual change in flow smoothness. The observed change in smoothness between serum stimulation (**c**) and starvation (**d**) in case of DNA probing in a representative nucleus. Time lag is 15 s starting from time point $t = 4$ s. Scale bars are $2\ \mu\text{m}$ and $0.2\ \mu\text{m}$ for the nuclei and zoomed in areas, respectively.

References

1. Horn BKP, Schunck BG (1981) Determining optical flow. *Artif Intell* 17(1–3):185–203.
2. Lucas BD, Kanade T (1981) An Iterative Image Registration Technique with an Application to Stereo Vision. *Imaging* 130(x):674–679.
3. Sun D, Roth S, Black MJ (2014) A quantitative analysis of current practices in optical flow estimation and the principles behind them. *Int J Comput Vis* 106(2):115–137.
4. Barron JL, Fleet DJ, Beauchemin SS (1994) Performance of optical flow techniques. *Int J Comput Vis* 12(1):43–77.
5. Karlsson SM, Bigun J (2012) Lip-motion events analysis and lip segmentation using optical flow. *IEEE Computer Society Conference on Computer Vision and Pattern Recognition Workshops*, pp 138–145.
6. Sveen JK (2004) An introduction to MatPIV v. 1.6.1. *Dep Math Univ Oslo, Oslo, Norw Eprint no.*(ISSN (809–4403)):1–27.
7. Gautama T, Van Hulle M a (2002) A phase-based approach to the estimation of the optical flow field using spatial filtering. *IEEE Trans Neural Networks* 13(5):1127–1136.
8. Liu C, Yuen J, Torralba A (2015) Sift flow: Dense correspondence across scenes and its applications. *Dense Image Correspondences for Computer Vision*, pp 15–49.
9. Rudin LI, Osher S, Fatemi E (1992) Nonlinear total variation based noise removal algorithms. *Phys D Nonlinear Phenom* 60(1–4):259–268.
10. Adrian RJ (2005) Twenty years of particle image velocimetry. *Experiments in Fluids*, pp 159–169.
11. Fleet DJ, Jepson AD (1990) Computation of component image velocity from local phase information. *Int J Comput Vis* 5(1):77–104.
12. Pauwels K, Van Hulle MM (2008) Mealttime phase-based optical flow on the GPU. *2008 IEEE Computer Society Conference on Computer Vision and Pattern Recognition Workshops, CVPR Workshops* doi:10.1109/CVPRW.2008.4563090.
13. Lowe DG (1999) Object recognition from local scale-invariant features. *Proc Seventh IEEE Int Conf Comput Vis* 2([8]):1150–1157.
14. Lowe DG (2004) Distinctive image features from scale-invariant keypoints. *Int J Comput Vis* 60(2):91–110.
15. Szeliski R, et al. (2008) A comparative study of energy minimization methods for Markov random fields with smoothness-based priors. *IEEE Trans Pattern Anal Mach Intell* 30(6):1068–1080.
16. Ovesný M, Křížek P, Borkovec J, Švindrych Z, Hagen GM (2014) ThunderSTORM: A comprehensive ImageJ plug-in for PALM and STORM data analysis and super-resolution imaging. *Bioinformatics* 30(16):2389–2390.
17. Metzler R, Jeon J-H, Cherstvy AG, Barkai E (2014) Anomalous diffusion models and their properties: non-stationarity, non-ergodicity, and ageing at the centenary of single particle tracking. *Phys Chem Chem Phys* 16(44):24128–64.

18. Zidovska A, Weitz D a, Mitchison TJ (2013) Micron-scale coherence in interphase chromatin dynamics. *Proc Natl Acad Sci U S A* 110(39):15555–60.
19. Shinkai S, Nozaki T, Maeshima K, Togashi Y (2016) Dynamic Nucleosome Movement Provides Structural Information of Topological Chromatin Domains in Living Human Cells. *PLoS Comput Biol* 12(10). doi:10.1371/journal.pcbi.1005136.
20. Stein ML (1999) *Interpolation of spatial data : some theory for kriging* (Springer) Available at: https://www.researchgate.net/publication/256715812_Interpolation_of_Spatial_Data_Some_Theory_for_Kriging_ML_Stein_Springer_New_York_1999_Hardcover_247_pp_US_4995_ISBN_0-387-98629-4 [Accessed September 17, 2017].
21. Minasny B, McBratney AB (2005) The Matern function as a general model for soil variograms. *Geoderma* 128(3–4):192–207.